

Construction and Properties of Ag-I Polymeric Clusters Attach With Nitrogen Heterocyclic Transition Metal Moiety

Min Liu

Liaoning Normal University

Yu Xin

Liaoning Normal University

Yong Heng Xing (✉ yhxing2000@yahoo.com)

Liaoning Normal University <https://orcid.org/0000-0002-7550-2262>

Fengying Bai

Liaoning Normal University

Zhan Shi

Jilin University

Research Article

Keywords: Silver cluster compounds, Electrochemistry, P-nitrophenol, Catalytic

Posted Date: November 9th, 2021

DOI: <https://doi.org/10.21203/rs.3.rs-1035422/v1>

License: © ⓘ This work is licensed under a Creative Commons Attribution 4.0 International License.

[Read Full License](#)

Version of Record: A version of this preprint was published at Journal of Inorganic and Organometallic Polymers and Materials on March 14th, 2022. See the published version at <https://doi.org/10.1007/s10904-022-02229-9>.

Abstract

Two silver cluster compounds $\{[\text{Co}(\text{1,10'-phen})_3]_2[\text{Ag}_8\text{I}_{12}]\}$ (**1**) and $\{[\text{Co}(\text{2, 2'-bipy})_3][\text{Ag}_{10}\text{I}_{11}](\text{OH})\cdot 3\text{DMF}\cdot 2\text{H}_2\text{O}\}$ (**2**) (1,10'-phen=1,10'-phenanthroline, 2, 2'-bipy=2,2'-bipyridine) were designed and synthesized by solvent evaporation method. The two silver cluster compounds were characterized by elemental analysis, infrared spectroscopy, ultraviolet spectroscopy, thermogravimetric analysis and X-ray powder diffraction. The crystal structures of compounds **1** and **2** were determined by X-ray crystallography diffraction. Through the electrostatic interaction between the metallic Ag cluster moiety and the metallic Co cluster moiety, form stable interlaced layered super molecular structures. In order to explore functional properties, the catalytic reduction of p-nitrophenol and electrochemical behavior of compounds **1** and **2** were explored. The results show that compounds **1** and **2** can efficiently catalyze the reduction of p-nitrophenol in the aqueous solution, and the reduction and removal rate can reach more than 90%.

Highlights

- Synthesis of compounds **1** and **2** characterized by single crystal X-ray crystallography in detail.
- **1** and **2** through the electrostatic interaction between the metallic Ag cluster moiety and the metallic Co cluster moiety, formed stable interlaced layered super molecular structures.
- **1** and **2** can efficiently catalyze the reduction of p-nitrophenol.

1. Introduction

Nowadays, with the rapid development of industry, agriculture, and handicrafts, a large amount of hazardous organic wastewater is discharged into the water, causing water pollution, destroying the environmental balance, and even threatening human life and health. Therefore, the development of a catalyst that can efficiently remove organic pollutants has become a current research hotspot^[1-2]. Catalytic technology is the process of degrading all the pollutants in the aqueous solution into non-toxic substances under the action of a catalyst. These compounds are usually toxic. Discharge into the water will cause water pollution and have carcinogenic effects on humans. Among the many pollutants, nitroaromatic compounds, especially nitrophenol compounds, account for a large proportion. Therefore, the removal of nitroaromatic compounds is particularly important^[3-5]. So, the degradation and catalytic reduction of p-nitrophenol (PNP) and other nitrophenol compounds have attracted great attention^[6-8]. As we know, p-nitrophenol (PNP) can be effectively reduced to p-aminophenol (PAP). PAP is an effective industrial intermediate, which can be used in analgesic and antipyretic drugs, imaging agents, antiseptic lubricants, etc. In 2016, Sá^[9] *et al.* used molecular hydrogen as a reducing agent for the first time to produce p-aminophenol by continuous flow hydrogenation of p-nitrophenol. This method is to convert a toxic substance into another non-toxic product through an oxidation-reduction reaction, and the by-product is only water, and water is also a solvent, which provides a new idea for removing p-nitrophenol. In 2016, Zhu^[10] *et al.* used Ni-Ca-Al₂O₃ to catalyze the reduction of p-nitrophenol (PNP). The mechanism

is that Ni-Ca-Al₂O₃ catalyzes the release of H₂ from NaBH₄, and then reduces PNP to p-aminophenol. In 2019, Chen^[11] *et al.* synthesized W-TiO₂/SiO₂ catalyst and studied that it can photo catalyze p-nitrophenol with a mineralization rate of about 99%. P-nitrophenol is first degraded into intermediates by light, and these intermediates are further degraded into smaller fragments such as organic carboxylic acids, and finally fully mineralized. It can be seen that catalytic technology is widely used in the treatment of organic pollutants, and its removal effect is also significant. In 2020, Feng^[12] *et al.* used nano-pyrite to catalytically reduce p-nitrophenol. Nano-pyrite is dissolved to release Fe²⁺ under acidic conditions, and then H₂O₂ is added. H₂O₂ produces a large amount of •OH under the action of Fe²⁺, and finally •OH catalyzes reduction of p-nitrophenol to produce CO₂ and H₂O. Eshaq^[13] *et al.* prepared a core-shell nanostructure FeVO₄@CeO₂, which was used as a catalyst to achieve the catalytic reduction and degradation of p-nitrophenol. Catalytic hydrogenation is a method in which NaBH₄, H₂O or C₂H₅OH is used as a hydrogen donor to provide active hydrogen for the catalytic process, and then the aromatic nitro compound is catalytically reduced to an aromatic amino compound^[14-17]. In 2020, Shimoga^[18] *et al.* studied the mechanism of silver nanoparticles (SNPs) catalyzing the PNP process: After sodium borohydride aqueous solution interacts with SNPs, hydrogen gas is rapidly generated and adsorbed on the surface of SNPs, thereby reducing p-nitrophenol on the surface of SNPs. Today, materials such as nanomaterials, graphene, metal oxides and metal organic frameworks have been used as catalysts for the catalytic reduction of p-nitrophenol^[19-21]. Among them, the metal-organic framework has the characteristics of high surface area, high porosity, high stability, etc., which has attracted wide attention. Therefore, looking for an efficient metal-organic framework catalyst has become one of the future research directions.

Nitrogen heterocyclic complexes are metal organic frameworks with specific structures formed by using nitrogen heterocyclic organic compounds as ligands and connecting with the central metal. A simple nitrogen heterocyclic ring is an organic compound containing a five-membered or six-membered heterocyclic structure in the molecule, which means that there is at least one nitrogen atom in the heterocyclic ring^[22]. Nitrogen heterocyclic ligands can form π-π interactions between rings to further stabilize the structure of the complex^[23-27]. In 2016, Cheng^[28] *et al.* synthesized [Ru(bpy)₂]₃(μ₃-L²) (PF₆)₆ (bpy=2,2'-bipyridine), and studied its photophysical and electrochemical properties. In 2017, Bedowr^[29] *et al.* synthesized [Cu(η¹-(OOCR)₂(2,2'-bpy) (4,4'-bpy)](2,2'-bpy=2,2'-bipyridine, 4, 4'-bpy=4,4'-bipyridine), and its magnetic properties were studied. In 2018, Gaml^[30] *et al.* synthesized the complex [Ru(bpy)₂(Hapbim)]²⁺ (bpy=2,2'-bipyridine, Hapbim is 2-aminophenylbenzimidazole), and measured it by spectrophotometry Optical properties. In 2019, Doyle^[31] *et al.* synthesized {[Hphen][Fe(phen) (H₂P₂O₇)₂·2H₂O} (phen=1,10'-phenanthroline) and studied its magnetic properties. Yakhvarov^[32] *et al.* synthesized new nickel phosphate complexes [Ni(HPO₄)(bpy)₂] and [Ni(HPO₄)(phen)₂]. The X-ray crystal structure analysis of the complexes showed that the nickel ions have a twisted octahedral complex. The complex structure and diverse functions of silver clusters have attracted wide attention. In 2016, An^[33] *et al.* used the fluorescence enhancement of the silver nanocluster complex to efficiently detect Ca²⁺. In

2017, Zang^[34] *et al.* connected the silver cluster complexes to adaptable ligands to connect them to each other and form a rigid metal-organic framework. Multi-color lights made of volatile organic compounds that are triggered off by oxygen. In 2018, Liang^[35] *et al.* stated in a review that several silver complexes have antibacterial, antifungal, anticancer and other biological activities. In 2020, Weng^[36] *et al.* designed a thermally fluorescent color-changing elastic polymer film by incorporating silver nanoclusters. The color of the polymer film changes when the temperature is higher than 120 °C, and the fluorescence was enhanced. At present, the silver cluster compounds are still under continuous research.

Therefore, two silver cluster compounds $\{[Co(1, 10'\text{-phen})_3]_2[Ag_8I_{12}]\}$ (**1**) and $\{[Co(2,2\text{-bipy})_3][Ag_{10}I_{11}](OH)3DMF2H_2O\}$ (**2**) were designed and synthesized based on 1, 10'-phenanthroline and 2, 2'-bipyridine ligands by solvent evaporation method, the electrochemical behavior of **1** and **2** and the optimal resting time, pH and sweep rate of the cyclic voltammetry curve were studied. The catalytic reduction of PNP was also explored, and the catalytic reduction of PNP was also investigated. The mechanism of the process was speculated, the reduction and removal rate can reach more than 90%.

2. Experimental

2.1 Materials and method: All chemicals purchased were of reagent grade or better and were used without further purification. Solvents were purified according to the standard methods. The instrument used in this work is in the supporting information.

2.2 Preparation of **1** and **2**

In this work, 1,10'-phenanthroline and 2,2'-bipyridine were used as ligands, AgI_2^- was used as the metal source, and the silver cluster compounds **1** and **2** was synthesized by solvent volatilization under the conditions of DMF solvent. The detailed preparation methods of **1** and **2** were described in the supporting information. The synthetic route for the compounds **1** and **2** were summarized in Scheme 1.

2.3 Fabrication of electrodes

The BCPE was made by 0.75 g of graphite powder and 0.25 g of paraffin wax. Mixed the two evenly, after 3 times of heating and grinding, put them into a self-made glass tube with a diameter of 3 mm, and finally insert a copper wire^[37-38]. The same process to prepare the working electrode. During the grinding, add 10 mg of the compound was added to the carbon paste.

Cyclic voltammetry uses a three-electrode system: the reference electrode is a saturated calomel electrode, the counter electrode is a platinum electrode, the working electrode is a carbon paste electrode, and the electrolyte solution is a 1 M KCl solution. Measure cyclic voltammetry curves at different scanning speeds, different static times and different pH value^[39].

2.4 Catalytic experiment of compounds

Add 20 mL PNP solution and 2 mL NaBH₄ solution together, the solution turns bright yellow, and then add a certain amount of compound and ultrasonic for 30 s, and measure the absorbance of the solution at a specific wavelength at different time intervals with an ultraviolet-visible spectrophotometer, calculate the reduction rate of PNP. Figure S1 was standard curve of PNP solution.

3. Results And Discussion

3.1 IR spectra

The IR spectra of a series of the complexes were shown in Figure S2. In the IR spectrum of **1**, the characteristic peak at 1673 cm⁻¹ is attributed to the C=N stretching vibration, while the C=N stretching vibration peak of the ligand 1, 10'-phen is at 1654 cm⁻¹. The C=N stretching vibration peak of **1** is red-shifted compared to the C=N stretching vibration peak of ligand 1, 10'-phen, which indicates that the metal Co(III) is coordinated with the ligand. In the IR spectrum of **2**, the vibration peak at 1663 cm⁻¹ is considered to be the stretching vibration of C=N, while the C=N stretching vibration of ligand 2, 2,2'-bipy appears at 1665 cm⁻¹. The C=N stretching vibration of **2** is blue-shifted compared to the C=N stretching vibration peak of ligand 2, 2,2'-bipy, which indicates that the metal Co(III) is coordinated with the ligand. The main infrared data were listed in **Table S3**.

3.2 UV-vis spectra

The UV-Vis spectra of a series of the compounds were shown in Figure S3. The π - π^* transition and n - π^* transition of the ligand 1, 10'-phen appear at 256 nm and 325 nm. For **1**, the two strong absorption bands at 220 nm and 261 nm were attributed to the ligand-to-ligand charge transition (LLCT). The strong absorption band at 376 nm can be attributed to the ligand-to-metal charge transition (LMCT). It further shows that the metal Co(III) is coordinated with the ligand 1, 10'-phen. The two strong absorption bands at 218 nm and 321 nm are the π - π^* and n - π^* transitions of **2**, which can be attributed to the ligand-to-ligand charge transition (LLCT). The π - π^* transition and n - π^* transition of the ligand 2, 2,2'-bipy appear at 264 nm and 316 nm. The strong absorption band at 411 nm can be attributed to the ligand-to-metal charge transition (LMCT). It further shows that the metal Co(III) is coordinated with the ligand 2, 2,2'-bipy. Due to the wavelength limitation of the instrument, the characteristic absorption peak of Co is not shown. The main UV-vis spectra data were listed in **Table S4**.

3.3 Powder X-ray diffraction (PXRD)

The experimental and simulated PXRD patterns of **1** and **2** are shown in Figure S4. As shown in the Figure S4a and Figure S4b, although the peak intensity of the experimental PXRD pattern and the simulated PXRD pattern are slightly different, the positions of the respective peaks are almost the same. This indicates that **1** and **2** are pure phase without impurities. At the same time, as shown in Figure S5a and Figure S5b, the crystallinity of **1** and **2** was calculated according to the jade 5 software, which were 54.62 % and 74.65 %, respectively.

3.4 Thermogravimetric analyses (TG)

To verify the thermal stability of the compound, thermogravimetric analysis was performed at a heating rate of 10°C/min under a N₂ atmosphere with the temperature range from 30 to 800°C. The TG curve of **1** was shown in Figure S6a, the first stage of weight loss occurs at 30-560 °C, and the actual weight loss rate is 29.6% (theoretical weight loss rate: 30.1%), which corresponds to the loss of six 1,10'-phen ligands. The second weight loss stage occurs at 560-800 °C, the actual weight loss rate is 8.6%, which corresponds to the collapse of the framework, and the final residue was metal oxide. The TG curve of **2** was shown in Figure S6b, the first stage of weightlessness occurs at 30-150 °C, and the actual weight loss rate is 1.7% (theoretical weight loss rate: 1.6%), which corresponds to the loss of two water and a hydroxide ion. The second stage of weight loss occurs at 150-530 °C, and the actual weight loss rate is 16.9% (theoretical weight loss rate: 16.0%), which corresponds to the loss of three DMF and three 2,2'-bipy. The third weight loss stage occurs at 530-800 °C, the actual weight loss rate is 6.0%, which corresponds to the part collapse of the framework, and the final residue was metal oxide. Comparing the weight loss of **1** and **2**, the thermal stability of **2** is relatively better. The main thermogravimetric analyses data were listed in **Table S5**.

3.5 Crystal structures of the compounds **1** and **2**

Compound **1** belongs to the monoclinic system with $P2_1/c$ space group. The molecular structure includes a metallic Ag cluster and a Co cluster dimer with six 1,10'-phen. The metal Co atom chelates with six nitrogen atoms (N1-N6) from three 1,10'-phen to form a six-coordinate octahedral configuration, as shown in Fig.1a. The coordination mode of ligand 1, 10'-phen is $\mu_2\text{-}\eta_N^1\eta_N^1$, as shown in Fig.1c. The Ag clusters consist of eight silver ions and twelve iodide ions, as shown in Fig.1b.

In the Ag cluster, both Ag1 and Ag2 form a deformed triangular pyramid structure, Ag1 is coordinated by two $\mu_2\text{-I}$ (I2, I8) and one $\mu_3\text{-I}$ (I3), Ag2 is coordinated by two $\mu_2\text{-I}$ (I1, I2) and one $\mu_3\text{-I}$ (I4). Among them, Ag3, Ag4, Ag5, Ag6, Ag7 and Ag8 all form a twisted tetrahedral configuration, Ag3 is coordinated by two $\mu_2\text{-I}$ (I1, I12) and two $\mu_3\text{-I}$ (I3, I5), Ag4 is coordinated by three $\mu_3\text{-I}$ (I3-I5) and one $\mu_4\text{-I}$ (I6), and Ag5 is coordinated by two $\mu_2\text{-I}$ (I7, I8), one $\mu_3\text{-I}$ (I4) and one $\mu_4\text{-I}$ (I6), Ag6 is coordinated to one $\mu_2\text{-I}$ (I10), two $\mu_3\text{-I}$ (I5, I11) and one $\mu_4\text{-I}$ (I6), Ag7 is coordinated to two $\mu_2\text{-I}$ (I7, I9), one $\mu_3\text{-I}$ (I11) and one $\mu_4\text{-I}$ (I6), Ag8 is coordinated to three $\mu_2\text{-I}$ (I9, I10, I12) and one $\mu_3\text{-I}$ (I11). The coordination environment of metallic Ag ions is shown in **Table S6**. The bond length range of Ag-I bond in compound **1** is about 2.709-3.252 Å, which is similar to the bond length range of Ag-I bond 2.737-3.181 Å reported in the literatures^[40-42]. Six tetrahedral AgI₄ and two triangular pyramid AgI₃ are connected by sharing edges to form Ag₈I₁₂ building block of Ag cluster. As shown in Fig. 1d, the Ag₈I₁₂ building blocks are connected by I₁₂ to form a one-dimensional chain structure. As shown in Fig. 1e and 1f, a more stable interlaced layered structure is formed between the metal Ag cluster part and the metal Co cluster part through the electrostatic interaction between the anion and the cation.

Compound **2** belongs to the monoclinic system with $C2/c$ space group. The molecular structure includes a metal Ag cluster, a metal Co cluster, a hydroxide ion, three free DMF and two lattice water. In the structure, the Co cluster is a cationic cluster with +2 valence. As shown in Fig. 2a, the metal Co atom and

six nitrogen atoms from three 2,2'-bipyridine (N1-N3, N1^{#1}-N3^{#1}; #1: 1-x, y, 0.5-z) form a six-coordinate octahedral configuration. As shown in Fig. 2c, the coordination mode of ligand 2, 2'-bipyridine is $\mu_2\text{-}\eta_N^1\eta_N^1$. Ag clusters are anionic clusters with -1 valence and consist of ten silver ions and eleven iodide ions as shown Fig. 2b. In which, Ag1 is coordinated by four $\mu_4\text{-I}$ (I1, I1^{#1}, I2, I2^{#1}) to form a tetrahedral configuration. Ag2 is coordinated by a $\mu_2\text{-I}$ (I4), a $\mu_3\text{-I}$ (I3) and a $\mu_4\text{-I}$ (I4) to form a deformed triangular pyramid configuration. Ag3 is coordinated by one $\mu_2\text{-I}$ (I4) and two $\mu_3\text{-I}$ (I5, I5^{#1}) to form a triangular pyramid configuration. Ag4 is coordinated by a $\mu_2\text{-I}$ (I4) and a $\mu_4\text{-I}$ (I6) to form a V shape. Ag5 is coordinated by one $\mu_3\text{-I}$ (I3) and six $\mu_4\text{-I}$ (I1, I1^{#1}, I2, I5, I6, I6^{#1}) to form a deformed pentagonal biconical configuration. Ag6 is coordinated by one $\mu_3\text{-I}$ (I3) and four $\mu_4\text{-I}$ (I1, I2, I5, I6) to form a triangular double cone configuration. The coordination environment of metallic Ag ions is shown in **Table S6**. The bond length range of Ag-I bond in compound **2** is 2.736-3.212 Å, which is similar to the bond length range of Ag-I bond (2.737-3.181 Å) reported in the literatures^[40-42]. Two V shaped AgI₂, three triangular pyramid configuration AgI₃, one tetrahedral configuration AgI₄, two triangular biconical configuration AgI₅ and two deformed pentagonal biconical configuration AgI₇ are connected by the sharing edges to form a "kite Shaped" Ag₁₀I₁₁ building block. As shown in Fig. 2d, the building blocks are connected by shared edges Ag3-I4 to form a one-dimensional chain structure. Similarly, like the structure of **1**, as shown in Fig. 2e and 2f, a more stable interlaced layered super molecular structure is formed between the metal Ag cluster part and the metal Co cluster part through the electrostatic interaction between the anion and the cation.

3.6 Electrochemical properties of **1** and **2**

Figure 3 is the CV curve of carbon paste electrode and compounds **1** and **2** electrode in NaOH electrolyte solution. Compared with the carbon paste electrode, the redox peak of **1** and **2** appeared. Fig. 3a is the CV curve of **1**, The oxidation peak is at 0.276 V and its current value is 2.696×10^{-7} A; the reduction peak is at -0.015 V and its current value is -2.407×10^{-7} A. Fig. 3b is the CV curve of **2**. The oxidation potential is at 0.261 V and the current value is 8.018×10^{-6} A; the reduction potential is at 0.039 V and the current value is -1.347×10^{-5} A. According to equation 1, it can be detected whether the electrode reaction is Nernst reaction. When $T = 298$ K, it can be simplified to $\Delta E_p = 59/z$. When the value of ΔE_p is close to $59/z$, the electrode reaction is a reversible reaction. The ΔE_p value of **1** is 251 mV, the ΔE_p value of **2** is 222 mV, and its ΔE_p value cannot be close to $59/z$, so the electrode reactions of **1** and **2** are all irreversible reactions. In an irreversible reaction, the number of transferred electrons in the oxidation process can be calculated by equation 2. According to equation 1, the number of transferred electrons of **1** and **2** is calculated to be 1.5 and 1.5, respectively. Therefore, the compounds **1** and **2** transfer 1.5 electrons during the oxidation process.

$$\Delta E_p = 2.3RT/zF \quad (1)$$

$$\left| E_p - E_{p/2} \right| = 47.7/(1-\alpha) n \quad (2)$$

Where ΔE_p is the difference between oxidation potential and reduction potential (mV), R is 8.314 J/(mol·K), T is temperature (K), z is the number of transferred electrons, F is 96500 C/mol, E_p is the oxidation peak Potential (mV), $E_p/2$ is the half-peak potential (mV), α is the electron transfer coefficient, which is approximately 0.5, and n is the number of transferred electrons.

The Influence of Different Scanning Speed on Cyclic Voltammetry

By studying the CV curves of **1** and **2** at different scan rates, the CV curve at the best scan rate was determined. It can be seen from Fig. 4 that with the increase of the sweep rate, the peak current of the reduction potential and the oxidation potential of **1** first increase to the maximum and then decrease. At a sweep rate of 0.05 V/s, the peak current of **1** reaches the maximum and the peak shape is complete. Therefore, the best sweep speed of the CV curve of **1** is 0.05 V/s. Fig. 5a and Fig. 5b are the CV curves of **2** at different sweep speeds. It can be seen from the figure that the reduction potential and the peak current of the oxidation potential of **2** increase with the increase of the sweep rate. When the sweep speed is 0.1 V/s, the peak current reaches the maximum and the peak shape is complete. Therefore, the best sweep rate for the CV curve of **2** is 0.1 V/s.

The Influence of Different Resting Time on Cyclic Voltammetry

Through the research on the CV curve of **1** and **2** under different resting time, the CV curve under the best resting time is determined. It can be seen from Fig. 6 that the peak currents of the oxidation potential and reduction potential of **1** gradually decrease and then almost remain unchanged when the resting time increases. When the rest time is equal to 5 s, the peak current of the CV curve of **1** reaches the maximum and the peak shape is complete. Therefore, the optimal resting time of the CV curve of **1** is 5 s. It can be seen from Fig. 7 that as the sweep rate increases, the peak current of **2** also decreases, and remains unchanged after decreasing to the minimum. When the sweep speed is 5 s, the peak current reaches the maximum and the peak shape is perfect. Therefore, the optimal resting time of the CV curve of **2** is 5 s.

The influence of different pH on cyclic voltammetry curve

The CV curves of **1** and **2** were tested under the condition of phosphate buffer solution of different pH to study the effect of pH on the CV curves of **1** and **2**. It can be seen from Fig. 8 that as the pH changes from 5 to 6, the peak current of the reduction potential and oxidation potential of **1** reaches the maximum; as the pH changes from 6 to 8, the peak current gradually decreases. Therefore, pH = 6 can be used as the optimal pH for the CV curve of **1**. It can be seen from Fig. 9 that with the increase of pH, the peak current of **2** also increases, increases to the maximum and then decreases. When the pH is 8, the peak current reaches the maximum and the peak shape is good. Therefore, the optimal pH of the CV curve of **2** is 8.

3.7 Catalytic reduction of PNP by **1** and **2**

After adding NaBH_4 to the PNP solution, the color changed to bright yellow and a characteristic peak appeared at 400 nm. This is because PNP is ionized under alkaline conditions, and a large amount of H^+ are released under the condition of the catalyst, and PNP is catalytically reduced to PAP. The

characteristic absorption peak of PAP is at 298 nm. As shown in Fig. 10, as time increases, the characteristic peak at 400 nm gradually decreases, while the characteristic peak at 298 nm gradually increases. This means that the concentration of PNP is gradually decreasing, and the concentration of PAP is increasing. It can be seen that PNP is catalytically reduced to PAP under the combined action of **1** and **2** and NaBH_4 , and the reduction rates of **1** and **2** can reach more than 90%.

The effect of different concentrations of sodium borohydride

Because NaBH_4 is a key parameter that controls the entire redox reaction, it is necessary to determine the optimal concentration of NaBH_4 . A series of catalytic reduction experiments were carried out under the conditions of NaBH_4 concentration of 0.1-0.4 M, PNP concentration of 0.1 mM and 5 mg of the compound. As shown in Fig. 11, when the NaBH_4 concentrations were 0.1 M, 0.2 M, and 0.4 M, the removal rates of PNP by the catalytic reduction of **1** were 95.7%, 94.4% and 97.4%, respectively. As the concentration of NaBH_4 increases, the removal rate of catalytic reduction of PNP does not change significantly. Taking into account the length of the reduction time, the optimal concentration of NaBH_4 for the catalytic reduction of PNP in **1** was determined to be 0.2 M. As shown in Fig. 12, when the NaBH_4 concentration is 0.1 M, 0.2 M, and 0.4 M, the removal rate of PNP by the catalytic reduction of **2** is 30.1%, 92.9%, and 99.3%, respectively. As the concentration of NaBH_4 increases, the removal rate of catalytic reduction PNP also increases, but the removal rate of 0.2 M and 0.4 M NaBH_4 does not change much. Taking into account the utilization of the compound, the optimal concentration of NaBH_4 for the catalytic reduction of PNP in **2** was determined to be 0.2 M.

The effect of different concentrations of PNP

In order to determine the optimal concentration of PNP in the catalytic reduction process, a series of catalytic reduction experiments were carried out under the condition that the NaBH_4 concentration was 0.2 M and the 5 mg compound was unchanged. As shown in Fig. 13, when the PNP concentrations were 0.05 mM, 0.1 mM, and 0.15 mM, the removal rate of PNP by the catalytic reduction of **1** was 97.0%, 94.4%, and 90.1%, respectively. As the PNP concentration increases, the removal rate of catalytic reduction PNP decreases, but the removal rate does not change much. The time for catalytic reduction of 0.15 mM PNP solution of **1** is 70 min, which is relatively long, while the time for catalytic reduction of both 0.05 mM and 0.1 mM PNP solutions is 15 min. Taking into account the length of the reduction time and the utilization of the compound, the optimal PNP concentration for the catalytic reduction of **1** was determined to be 0.1 mM. As shown in Fig. 14, when the PNP concentration is 0.05 mM, 0.1 mM, and 0.15 mM, the removal rate of PNP by the catalytic reduction of **2** is 100%, 92.9%, and 62.8%, respectively. With the increase of PNP concentration, the removal rate of PNP by the catalytic reduction of **2** decreases. When **2** is used for catalytic reduction of 0.05 mM PNP solution, the reduction time is 2 min, which does not make full use of the compound. When catalytic reduction of 0.15 mM PNP solution, the reduction time is longer and the reduction rate is lower. Taking into account the utilization of the compound and the

reduction removal rate, the optimal PNP concentration for the catalytic reduction of **2** was determined to be 0.1 mM.

The influence of the amount of different catalysts

In order to make full use of the reducibility of the compound, the optimal dosage of the compound in the catalytic reduction of PNP was determined. A series of catalytic reduction experiments were carried out under constant conditions of NaBH_4 concentration of 0.2 M and PNP concentration of 0.1 mM. As shown in Fig. 15, in the case of 3 mg, 5 mg, and 10 mg of **1**, the removal rates of catalytic reduction of PNP are 83.4%, 94.4%, and 97.7%, respectively. With the increase of the amount of **1**, the removal rate of catalytic reduction PNP increases, but the degree of removal rate changes little. Taking into account the length of the reduction time and the utilization of the compound, the optimal dosage of **1** was determined to be 5 mg. As shown in Fig. 16, in the case of 3 mg, 5 mg, and 10 mg of **2**, the removal rate of PNP by the catalytic reduction of **2** is 48.6%, 92.9%, and 100%, respectively. As the amount of **2** increases, the removal rate of catalytic reduction of PNP increases. When 10 mg of **2** is used for catalytic reduction of PNP solution, the reduction time is very short, and it is useless to make full use of the compound. When 3 mg of **2** is used for catalytic reduction of PNP solution, the reduction time is longer and the reduction rate is lower. Therefore, considering the utilization and reduction rate of the compound, the optimal dosage of **2** was determined to be 5 mg.

3.8 Kinetic Study of Catalytic Reduction Process

In order to analyze the kinetic behavior of the catalytic reduction of PNP solution by **1** and **2**, we used the quasi-first-order kinetic equation 3 and the quasi-second-order kinetic equation 4 to linearly fit the catalytic reduction process of PNP, and we obtained Fig. 17 and other related parameters Table 1.

$$\ln(C_t / C_0) = -k_1 t \quad (3)$$

$$1/C_t - 1/C_0 = k_2 t \quad (4)$$

Where C_e (mol/L) represents the equilibrium concentration, C_t (mol/L) represents the concentration at a certain moment, k_1 (min^{-1}) and k_2 ($\text{L}/(\text{mol}/\text{min})$) represent the rate constant respectively, t (min) is the reaction time.

It can be seen from Fig. 17 that the R^2 values of the pseudo-first-order kinetic equation fitted by the catalytic reduction of PNP by **1** and **2** are 0.9952 and 0.9901, respectively, which are closer to 1 than the R^2 value of the pseudo-second-order kinetic equation. This indicates that the catalytic reduction of PNP solution by **1** and **2** conforms to the quasi-first order kinetic model.

Table 1
Correlation data of pseudo-first-order and pseudo-second-order kinetics

Compounds	Pseudo first-order kinetics model		Pseudo secondary-order kinetics model	
	k_1 (min ⁻¹)	R^2	k_2 (g/(mg·min))	R^2
1	0.1797	0.9952	10.862	0.905
2	0.1044	0.9901	5.5104	0.9592

3.9 Study on the mechanism of catalytic reduction of PNP

In order to better understand the process of the catalytic reduction of PNP solution by **1** and **2**, we speculated on the mechanism of the catalytic reduction process. It can be seen from the above that the compounds **1** and **2** exhibits good redox properties. Therefore, the mechanism of the catalytic reduction of PNP by **1** and **2** is: i) The silver cluster in compound **1** and **2** oxidizes BH_4^- to BO_2^- and releases H^+ ; ii) H^+ further de-catalytically reduces the PNP solution^[43]. It becomes a PAP solution and emits hydrogen gas.

4. Conclusions

This work uses solvent evaporation method to design and synthesize two silver cluster compounds $\{\text{Co}(\text{1,10'-phen})_3\}_2[\text{Ag}_8\text{I}_{12}]$ (**1**) and $\{\text{Co}(\text{2, 2'-bipy})_3\}[\text{Ag}_{10}\text{I}_{11}](\text{OH})\cdot 3\text{DMF}\cdot 2\text{H}_2\text{O}$ (**2**). The compounds **1** and **2** form an infinite two-dimensional planar structure through the electrostatic interaction between anion and cation. Compounds **1** and **2** can efficiently catalytically reduce PNP in aqueous solution, and the reduction removal rate can reach more than 90%. At the same time, kinetic analysis showed that the catalytic reduction of PNP by **1** and **2** fits well with the quasi-first-order kinetic model. The redox properties of **1** and **2** were determined by cyclic voltammetry curve. Therefore, the mechanism of the catalytic reduction of PNP by **1** and **2** is that the silver cluster anion in **1** and **2** deoxidizes BH_4^- through its own oxidative property and releases H^+ , and then H^+ catalytically reduces PNP to PAP, which releases hydrogen. Therefore, the compounds **1** and **2** can be used as a reducing agent for efficiently removing PNP in aqueous solution, and has good application prospects.

Declarations

Conflicts of interest

There are no conflicts to declare.

Acknowledgments

This work was supported by the grants of the National Natural Science Foundation of China (No.21571091), Liaoning Normal University High-end Scientific Research Achievement Funding Program

(No. 21GDL003), and Open Project of State Key Laboratory of Inorganic Synthesis and Preparative Chemistry, College of Chemistry, Jilin University in China (No. 2020-10).

Supporting Information

The following files are available free of charge CCDC 2114111 and 2115232 contains the supplementary crystallographic data for this paper. These data can be obtained free of charge from The Cambridge Crystallographic Data Centre via www.ccdc.cam.ac.uk/data_request/cif. Full experimental details are presented in the Supporting Information.

Declaration of interests

☒ The authors declare that they have no known competing financial interests or personal relationships that could have appeared to influence the work reported in this paper.

☒ The authors declare the following financial interests/personal relationships which may be considered as potential competing interests:

The authors declared that they have no conflicts of interest to this work.

Credit author statement:

Min Liu, experiment, process data, writing; Yu Xin, reviewing; Yong Heng Xing, reviewing and editing, supervision; Feng Ying Bai, reviewing and editing, supervision; Zhan Shi, software.

References

1. P. Yang, T.T. Nie, J. Hu, H.Q. Ni, J.J. Shi, *Funct. Mater. Lett.* **13**, 1950091.1-1950091.3 (2020)
2. L. Tan, A.D. Tang, Y. Zou, M. Long, Y. Zhang, J.O. yang, J. Chen, *Sci. Rep.* **7**, 3281 (2017)
3. T.H. Zhao, F.H. Zhang, J. Zhou, X.Q. Zhao, *Comments Inorg. Chem.* **41**, 1–33 (2020)
4. P.P. Guo, M. Liu, L.L. Shi, *J. Solid State Chem.* **286**, 121247 (2020)
5. H.A. Alidağı, S.O. Tümay, A. Şenocak, S. Yeşilot, *Dyes Pigm.* **153**, 172–181 (2018)
6. Z.M. Shammi, A.H. Kianfar, M.M. Momeni, *J. Mater. Sci. Mater. Electron.* **31**, 14810–14822 (2020)
7. Y. Gu, Y.Q. Jiao, A.P. Wu, X.G. Zhou, B. Buhe, T.W. Yin, B.J. Jiang, Y. Qu, C.G. Tian, *Res. Chem. Intermed.* **43**, 4759–4779 (2017)
8. S. Alghool, H.F. Abd El-Halim, A.M. Mostafa, *J. Inorg. Organomet. Polym Mater.* **29**, 1324–1330 (2019)
9. C. Paun, G. Słowik, E. Lewin, J. Sá, *RSC Adv.* **6**, 87564–87568 (2016)
10. J. Feng, Q. Wang, D.L. Fan, L.R. Ma, D.L. Jiang, J.M. Xie, J.J. Zhu, *Appl. Surf. Sci.* **382**, 135–143 (2016)

11. U.A. Sánchez, L.F. Chen, J.A. Wang, L.E. Noreña, M. Asomoza, S. Solis, X.L. Zhou, Y.Q. Song, J. Liu, *Int. J. Photoenergy*, 2019, 1-13 (2019)
12. T. Liu, N. Chen, Y. Deng, F.X. Chen, C.P. Feng, *RSC Adv.* **10**, 15901–15912 (2020)
13. G. Eshaq, S.B. Wang, H.Q. Sun, M. Sillanpaa, *Journal of Hazardous Materials*, **382**, 121059.1-121059.14 (2020)
14. W.M. Zhang, Z.W. Zhou, X.Y. Shan, R. Xu, Q. Chen, G.Y. He, X.Q. Sun, H.Q. Chen, *New J. Chem.* **40**, 4769–4774 (2016)
15. J.Y. Du, Y. Zhao, J. Chen, P. Zhang, L.L. Gao, M.Q. Wang, C. Cao, W. Wen, C.Q. Zhu, *RSC Adv.* **7**, 33929–33936 (2017)
16. J.W. Sun, J.S. Xu, A. Grafmueller, X. Huang, C. Liedel, G. Algara-Siller, M. Willinger, C. Yang, Y.S. Fu, X. Wang, M. Shalom, *Appl. Catal. B Environ.* **205**, 1–10 (2017)
17. J.S. Wu, J.S. Wang, T.N. Wang, L.M. Sun, Y.C. Du, Y.L. Li, H.Y. Li, *Appl. Surf. Sci.* **466**, 342–351 (2019)
18. G. Shimoga, R.R. Palem, S.H. Lee, S.Y. Kim, *Metals* **10**, 1661 (2020)
19. A.R. Zeng, A.R. Zeng, *Water Air Soil Pollut.* **8**, 278.1-278.17 (2017)
20. M. Lei, W. Wu, S.L. Yang, X.G. Zhang, Z. Xing, F. Ren, X.H. Xiao, C.Z. Jiang, *Part. Part. Syst. Charact.* **33**, 212–220 (2016)
21. T.L. Guo, C. Wang, N.N. Zhang, Y. Zhang, T. Chen, X. Xing, Z.D. Lu, L.L. Wen, *Cryst. Growth Des.* **9**, 6217–6225 (2020)
22. Y. Chen, X.L. Chi, Y.C. Xu, X.C. Wang, D.R. Xiao, *Z. anorg. allg. Chem.* **642**, 128–133 (2016)
23. S.X. Zhao, J.S. Wu, W.Z. Chen, *J. Organomet. Chem.* **848**, 249–280 (2017)
24. K. Laxman, A. Kumar, M. Ravikanth, *Asian J. Org. Chem.* **9**, 162–180 (2020)
25. R. Lopes, Á Raya-Barón, M.P. Robalo, C. Vinagreiro, S. Barroso, M.J. Romão, L. Fernández, M.M. Pereira, B. Royo, *Eur. J. Inorg. Chem.* 2021, 22-29 (2020)
26. P. Sánchez, Martín Hernández-Juárez, Nuria Rendón, Joaquín López-Serrano, Laura L Santos, Eleuterio Álvarez, Margarita Paneque, Andrés Suárez. *Dalton Trans.* **49**, 9583–9587 (2020)
27. W.S. Ouyang, J.H. Rao, Y.B. Li, X.H. Liu, Y.P. Huo, Q. Chen, X.W. Li, *Adv. Synth. Catal.* **362**, 5576–5600 (2020)
28. F.X. Cheng, S.W. Yu, M.L. Ren, C.X. He, H.J. Yin, *Transit. Met. Chem.* **41**, 305–314 (2016)
29. N.S. Bedowr, R.B. Yahya, N. Farhan, *J. Saudi Chem. Soc.* **22**, 255–260 2018
30. S.A. Elsayed, E.A. Gaml, M.A. Nasher, *Opt. Mater.* **84**, 8–15 (2018)
31. T.J. Greenfield, M.M. Turnbull, J. Zubieta, R.P. Doyle, *Inorg. Chim. Acta* **498**, 119084 (2019)
32. Z.N. Gafurov, A.B. Dobrynin, I.F. Sakhapov, A.A. Kagilev, A.O. Kantyukov, A.A. Balabaev, A.V. Toropchina, O.G. Sinyashin, D.G. Yakhvarov, *Phosphorus Sulfur Silicon Relat. Elem.* **194**, 517–521 (2019)
33. L. Lu, X.Q. An, W.X. Huang, *Anal. Methods* **9**, 23–27 (2017)

34. R.W. Huang, Y.S. Wei, X.Y. Dong, X.H. Wu, C.X. Du, S.Q. Zang, T.C.W. Mak, *Nat. Chem.* **9**, 689–697 (2017)
35. X.X. Liang, S.X. Luan, Z.Q. Yin, M. He, C.L. He, L.Z. Yin, Y.F. Zou, Z.X. Yuan, L.X. Li, X. Song, C. Lv, W. Zhang, *Eur. J. Med. Chem.* **157**, 62–80 (2018)
36. L.B. Wang, H. Chen, Q.Y. Yin, J. Kang, B. Liu, G.S. Weng, J. He, *Nanotechnology* **31**, 245703 (2020)
37. T.S. Sunil Kumar Naik, B.E. Kumara Swamy, *J. Electroanal. Chem.* **826**, 23–28 (2018)
38. M. Kumar, M. Wang, B.E. Kumara Swamy, M. Praveen, W. Zhao, *Colloids Surf. B Biointerfaces* **196**, 111299 (2020)
39. K. Chetankumar, B.E. Kumara Swamy, S.C. Sharma, *Mater. Chem. Phys.* **252**, 123231 (2020)
40. D.D. Yang, W.L. Xu, X.W. Cao, S.J. Zheng, J.G. He, Q. Ju, Z.L. Fang, W. Huang, *Inorg. Chem.* **16**, 7954–7961 (2016)
41. J.J. Shen, C.F. Zhang, T.L. Yu, L. An, Y.L. Fu, *Cryst. Growth Des.* **12**, 6337–6342 (2014)
42. Q. Wei, D. Wang, J. Pan, S.D. Han, G.M. Wang, *Chem. Asian. J.* **14**, 640–646 (2019)
43. C. Kästner, A.F. Thünemann, *Langmuir* **29**, 7383–7391 (2016)

Figures

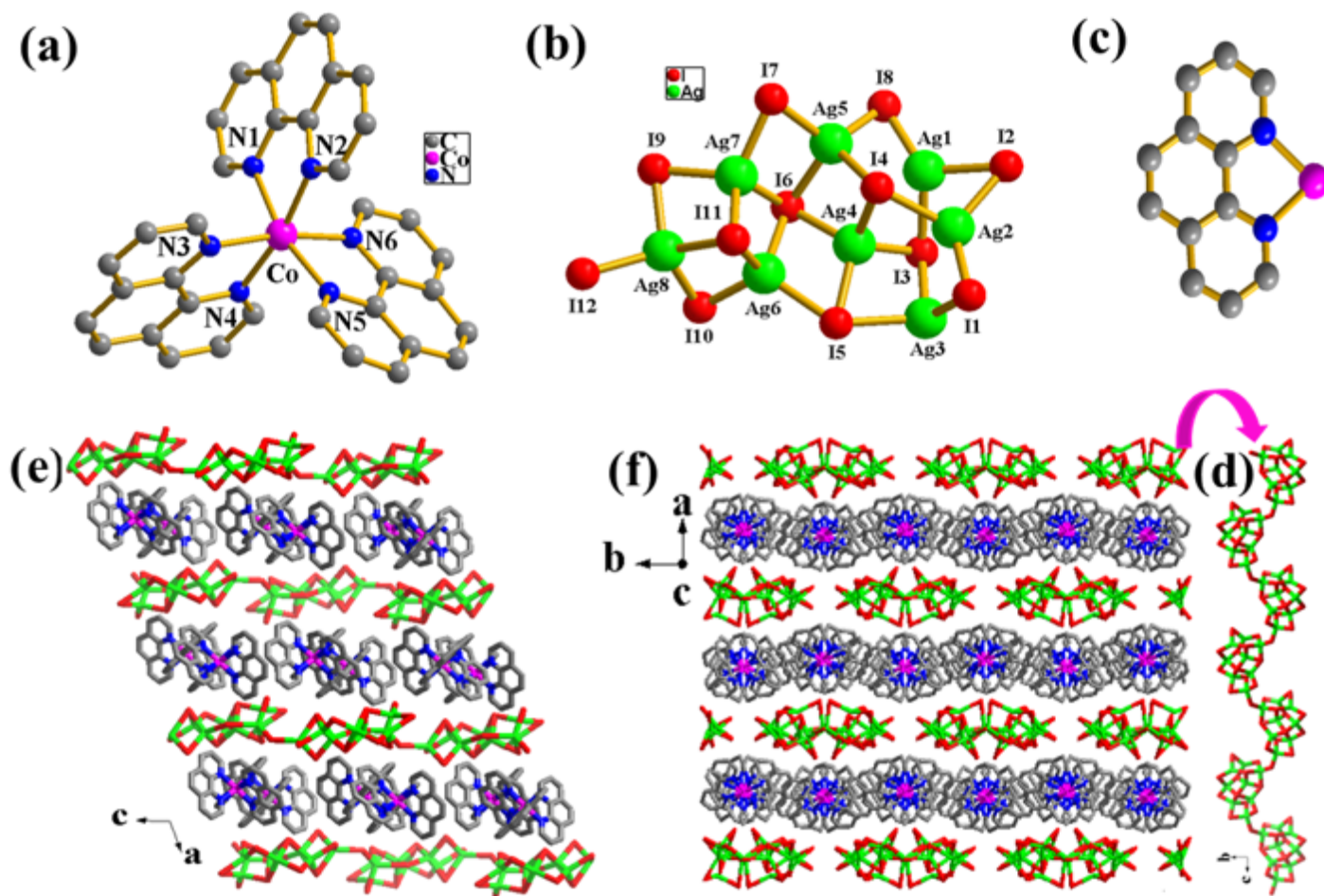


Figure 1

Compound 1: (a) The coordination environment of metal Co; (b) The coordination environment of metal Ag; (c) The connection mode of ligand phen; (d) 1D chain structure; (e) 2D layered structure; (f) 2D layered structure

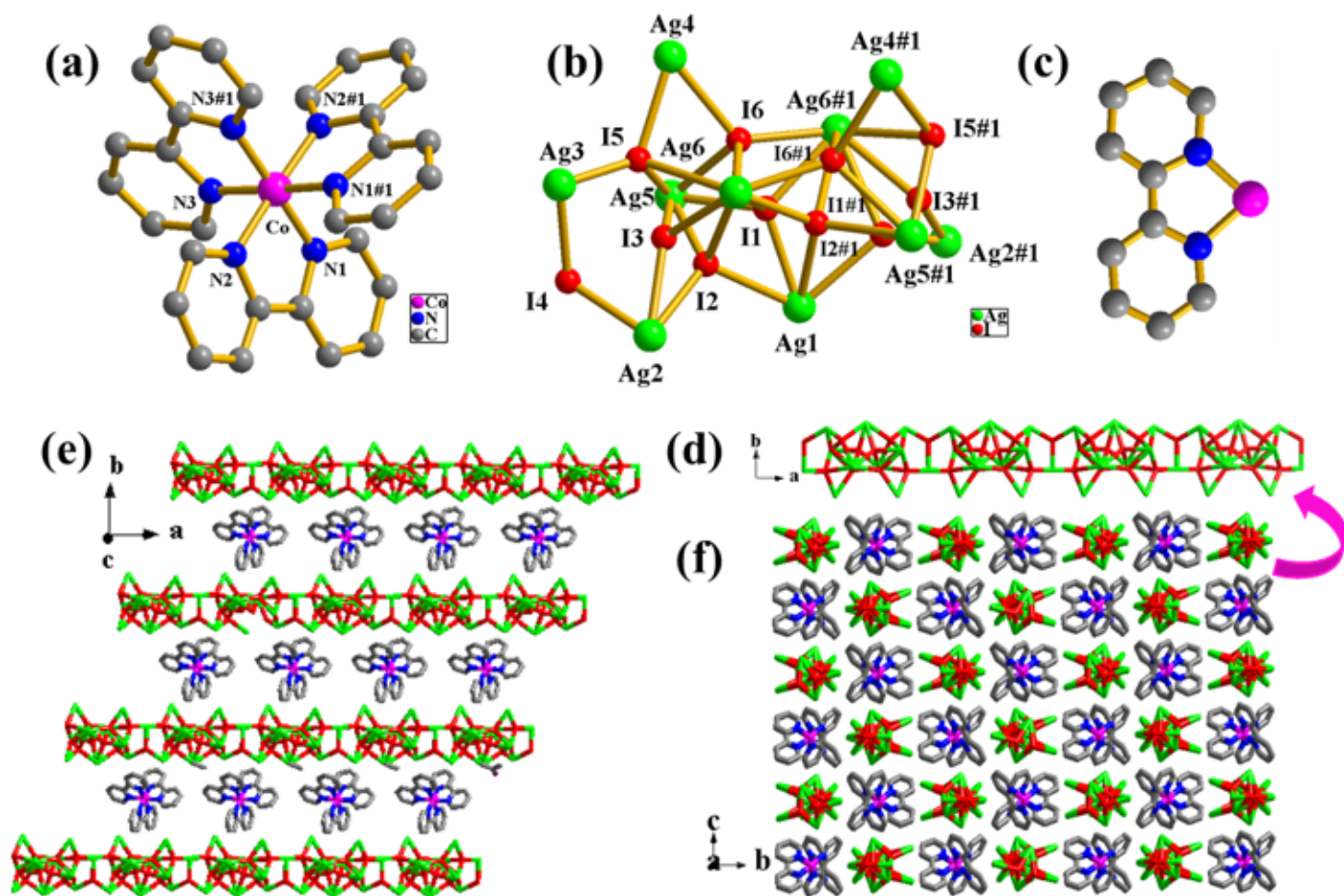


Figure 2

Compound 2: (a) The coordination environment of metal Co; (b) The coordination environment of metal Ag; (c) The connection of ligand 2, 2'-bipy; (d) 1D chain structure; (e) 2D layered structure (#1: 1-x, y, 0.5-z); (f) 2D layered structure (#1: 1-x, y, 0.5-z)

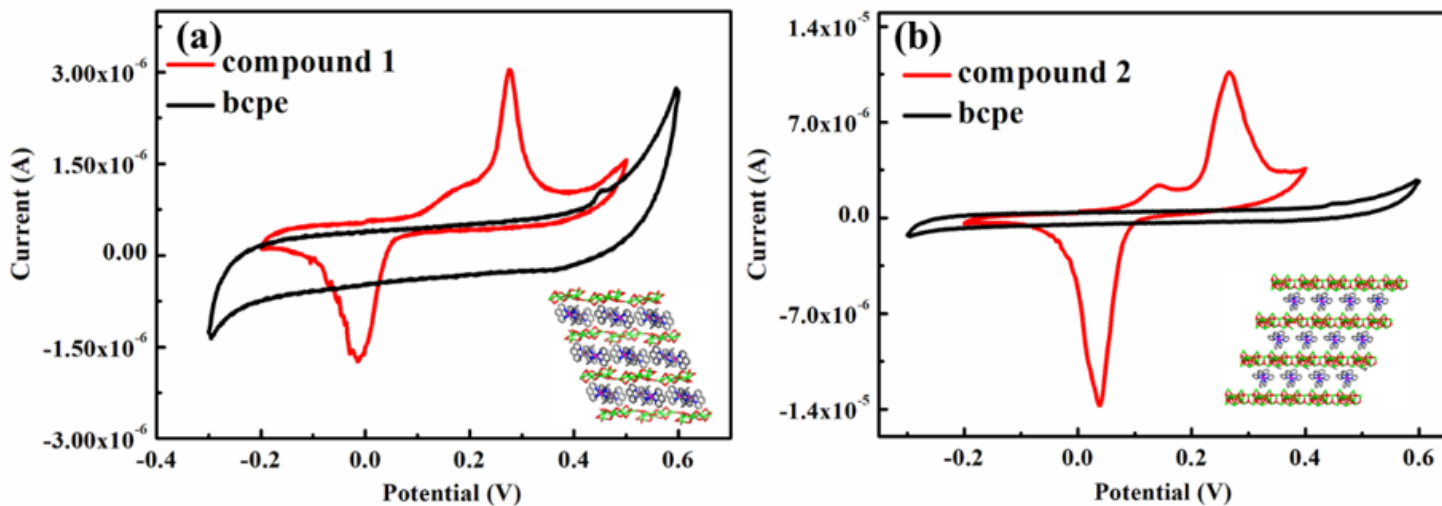


Figure 3

CV curves of bcpe and 1 and 2

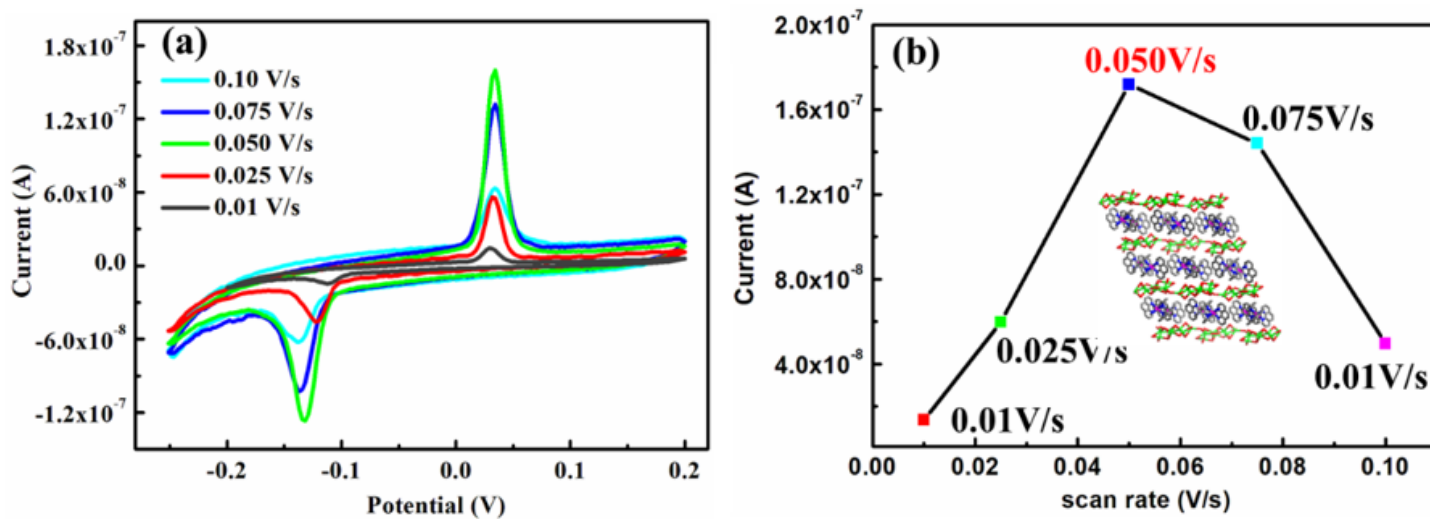


Figure 4

(a) CV curves of 1 at different scan rates; (b) The line chart of peak current at different scan rates of 1

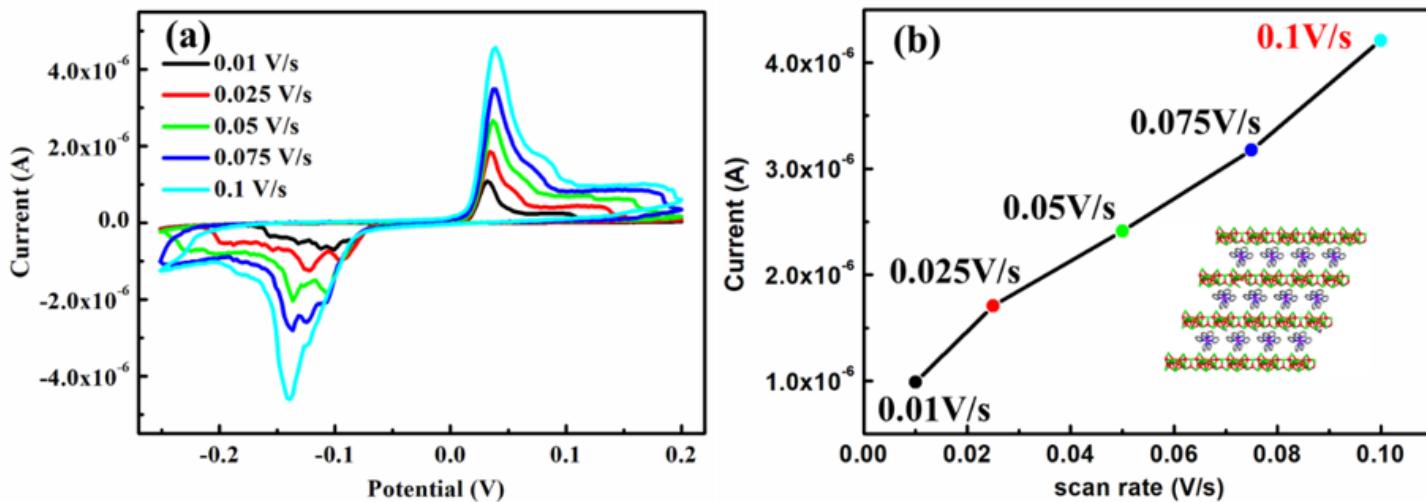


Figure 5

CV curves of 2 at different scan rates; (b) The line chart of peak current at different scan rates of 2

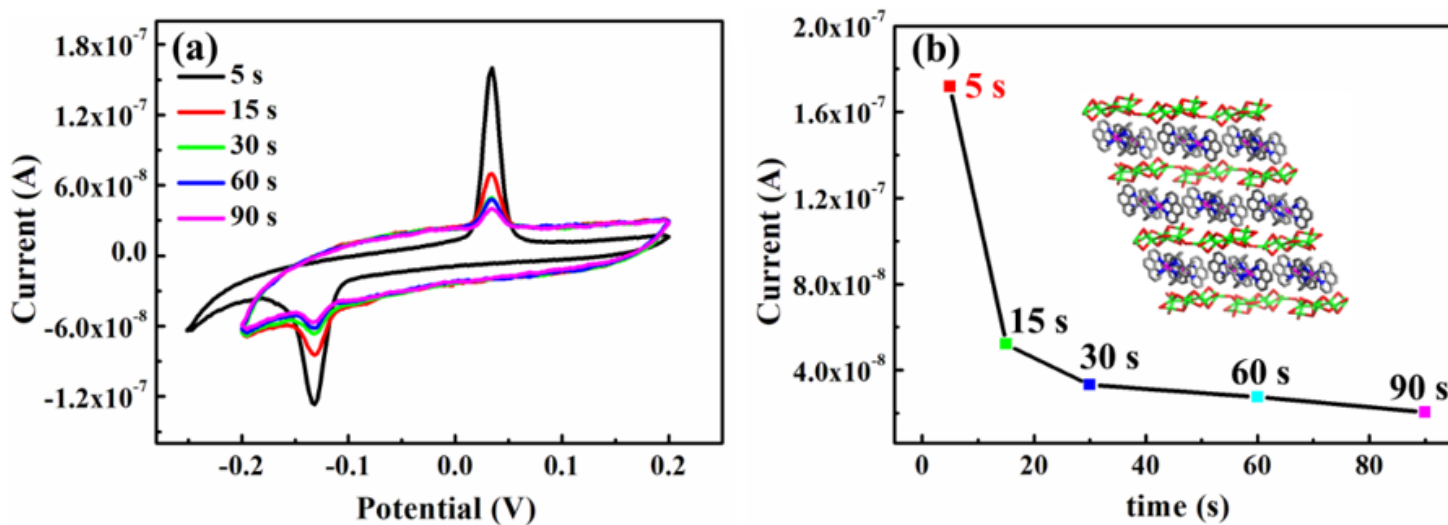


Figure 6

(a) CV curves of 1 at different time; (b) The line chart of peak current at different time of 1

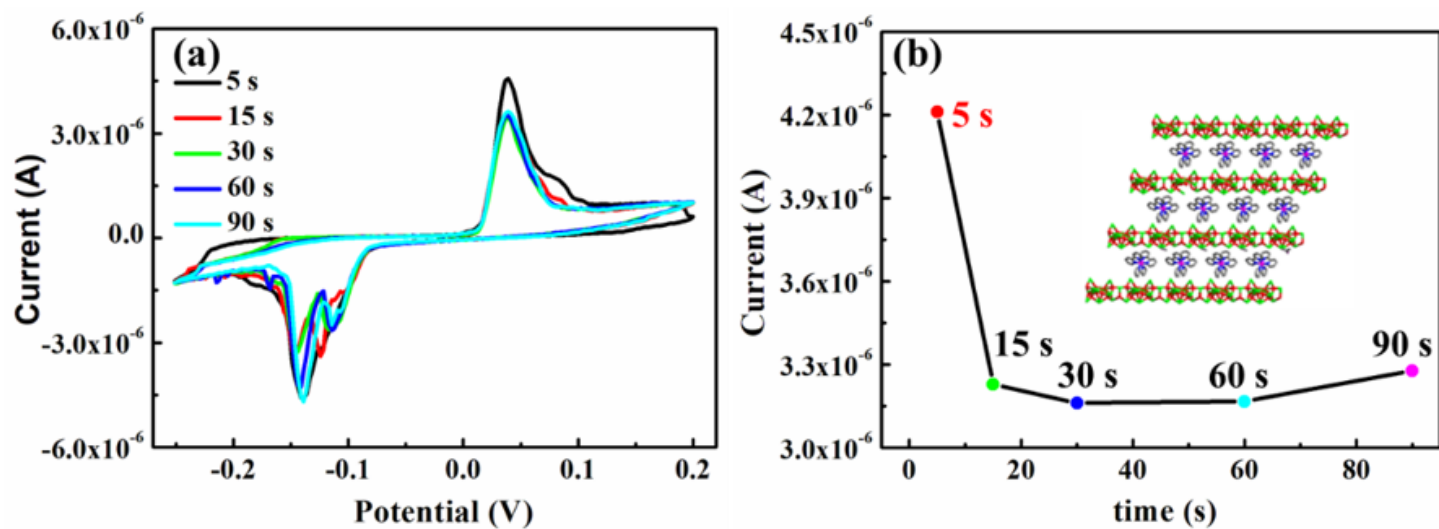


Figure 7

(a) CV curves of 2 at different time; (b) The line chart of peak current at different time of 2

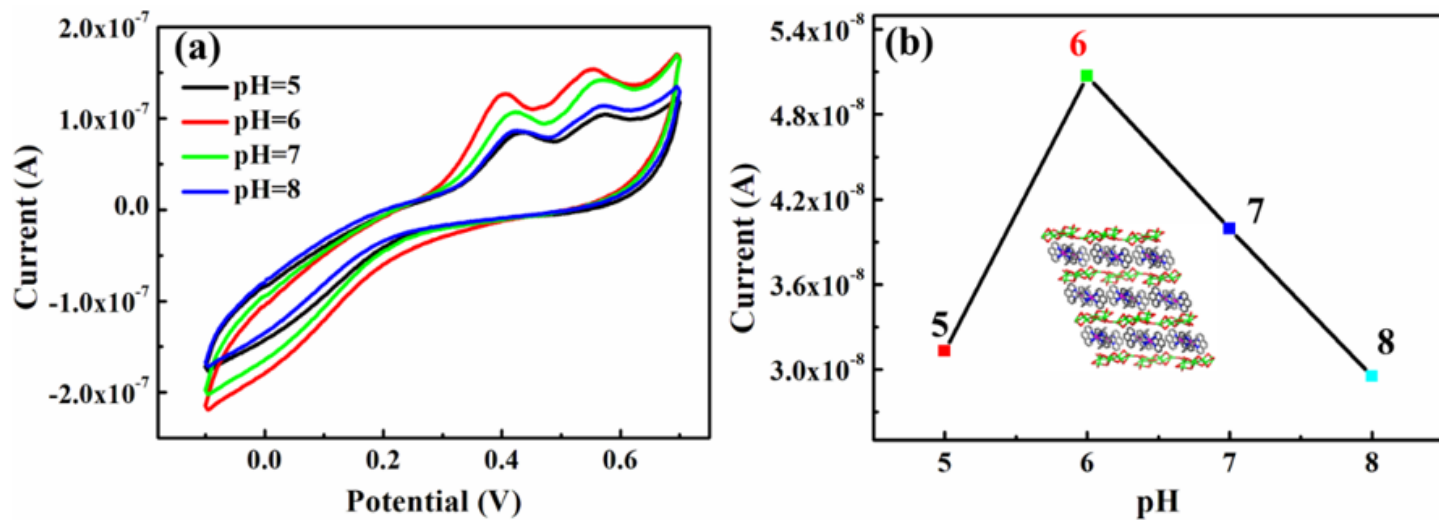


Figure 8

(a) CV curves of 1 at different pH; (b) The line chart of peak current at different pH of 1

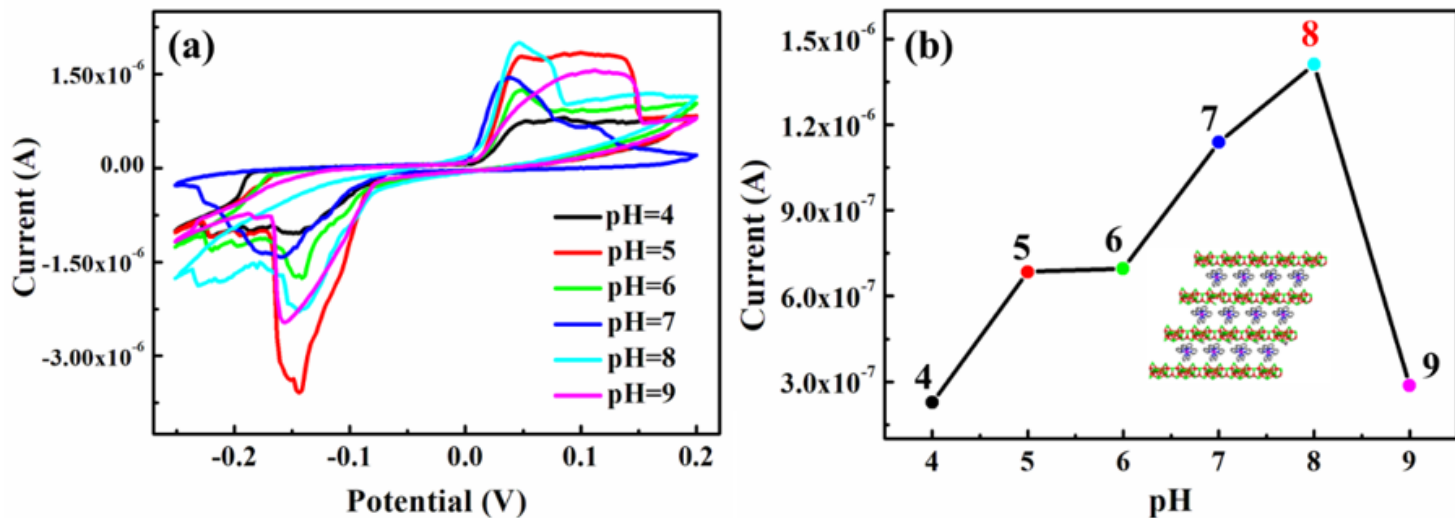


Figure 9

(a) CV curves of 2 at different pH; (b) The line chart of peak current at different pH of 2

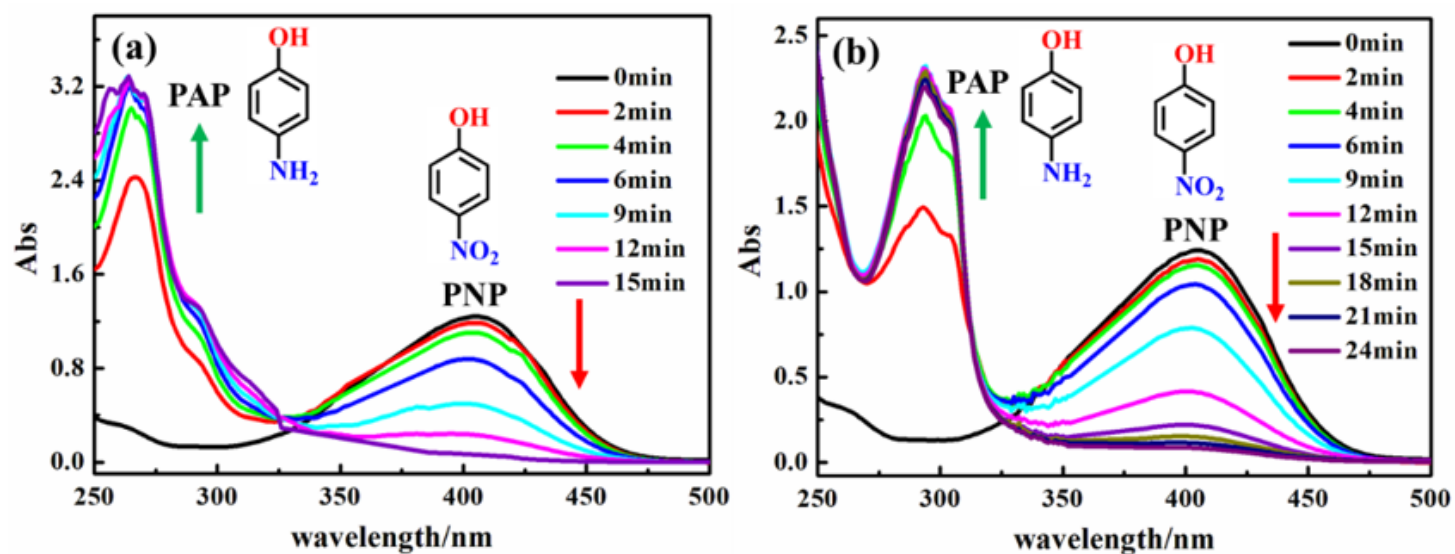


Figure 10

Curves of catalytic reduction of PNP: (a) 1; (b) 2

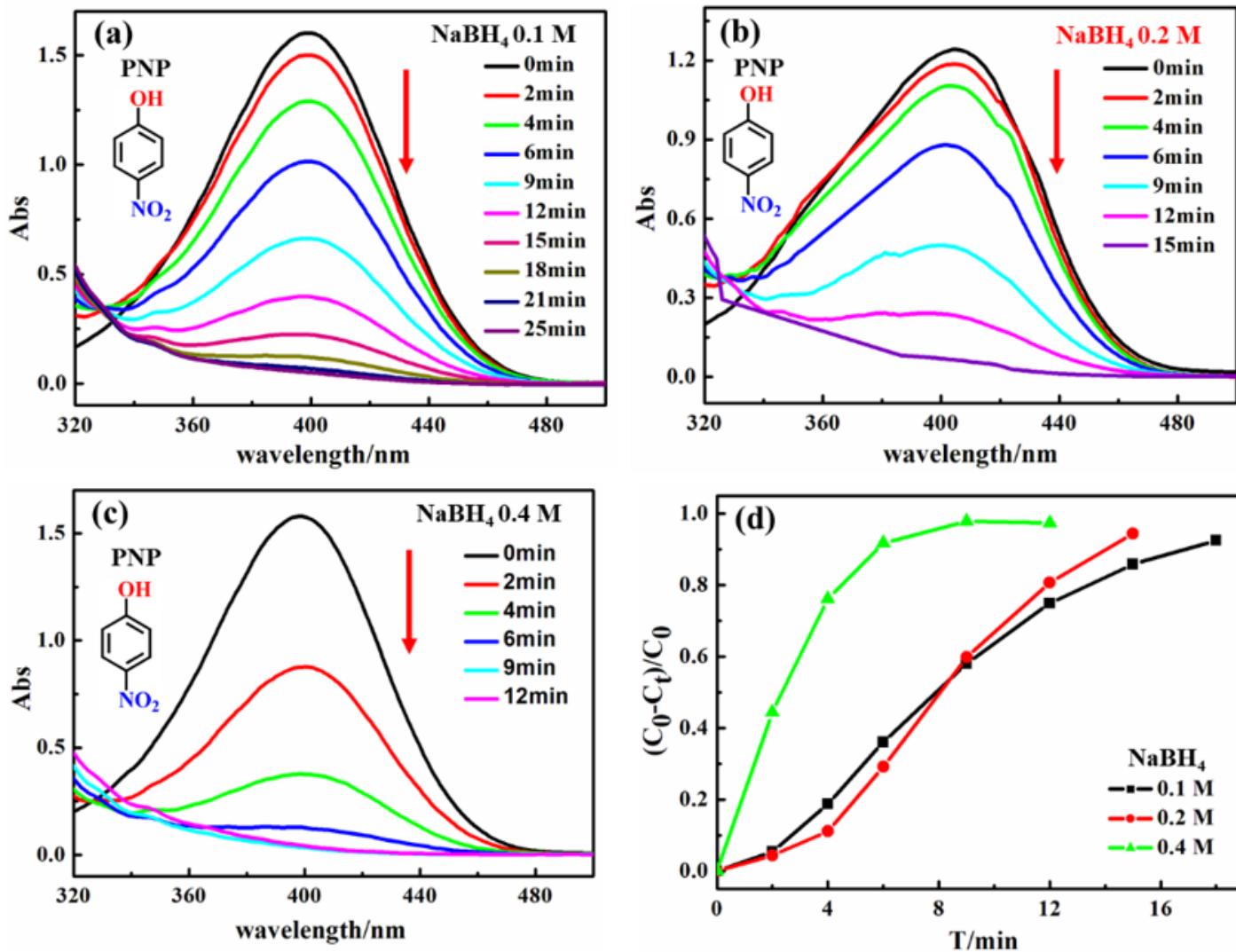


Figure 11

Effect of NaBH₄ concentration on catalytic reduction of PNP with 1: (a) 0.1 M; (b) 0.2M; (c) 0.4 M; (d) Comparison of removal rates

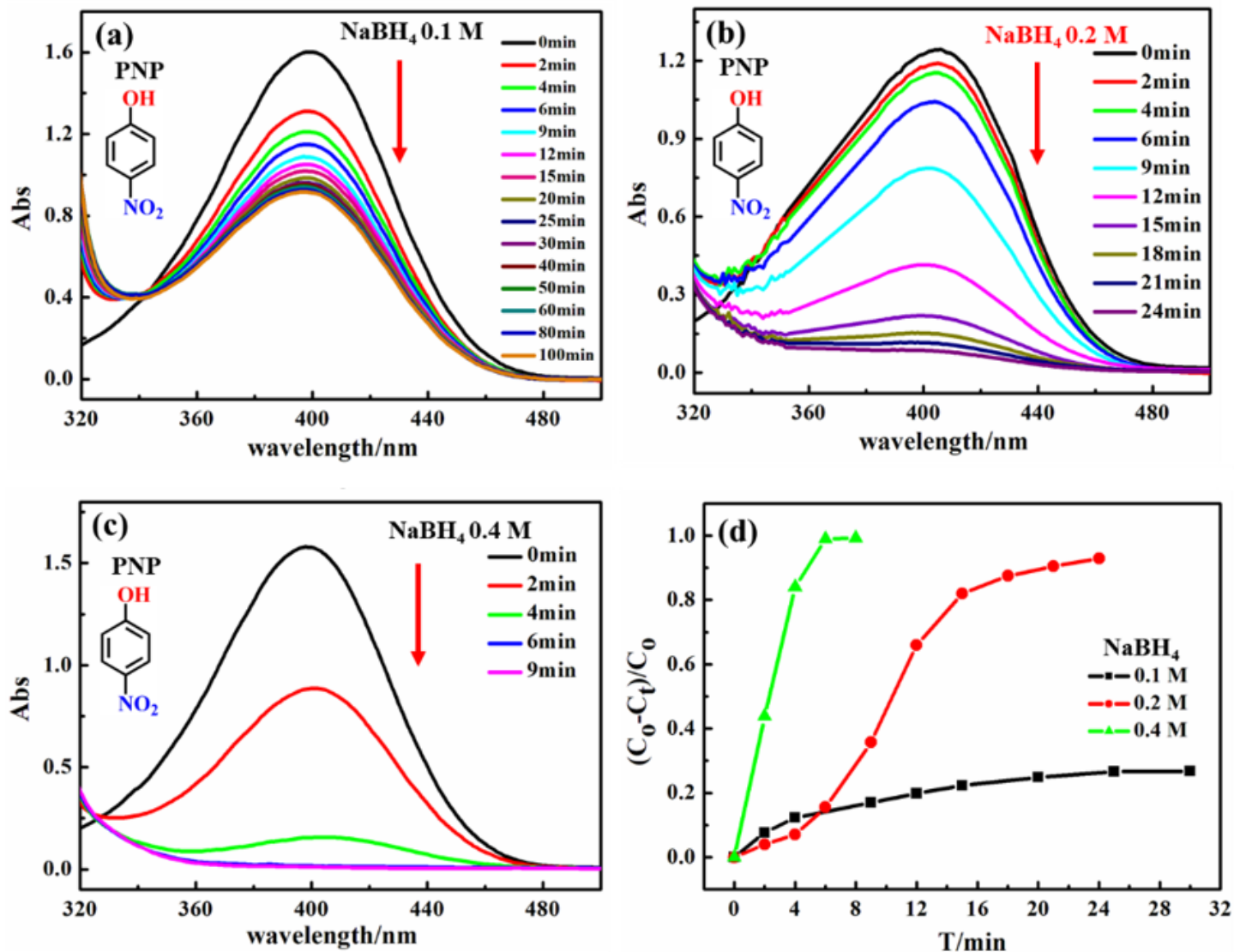


Figure 12

Effect of NaBH₄ concentration on catalytic reduction of PNP with 2: (a) 0.1 M; (b) 0.2M; (c) 0.4 M; (d) Comparison of removal rates

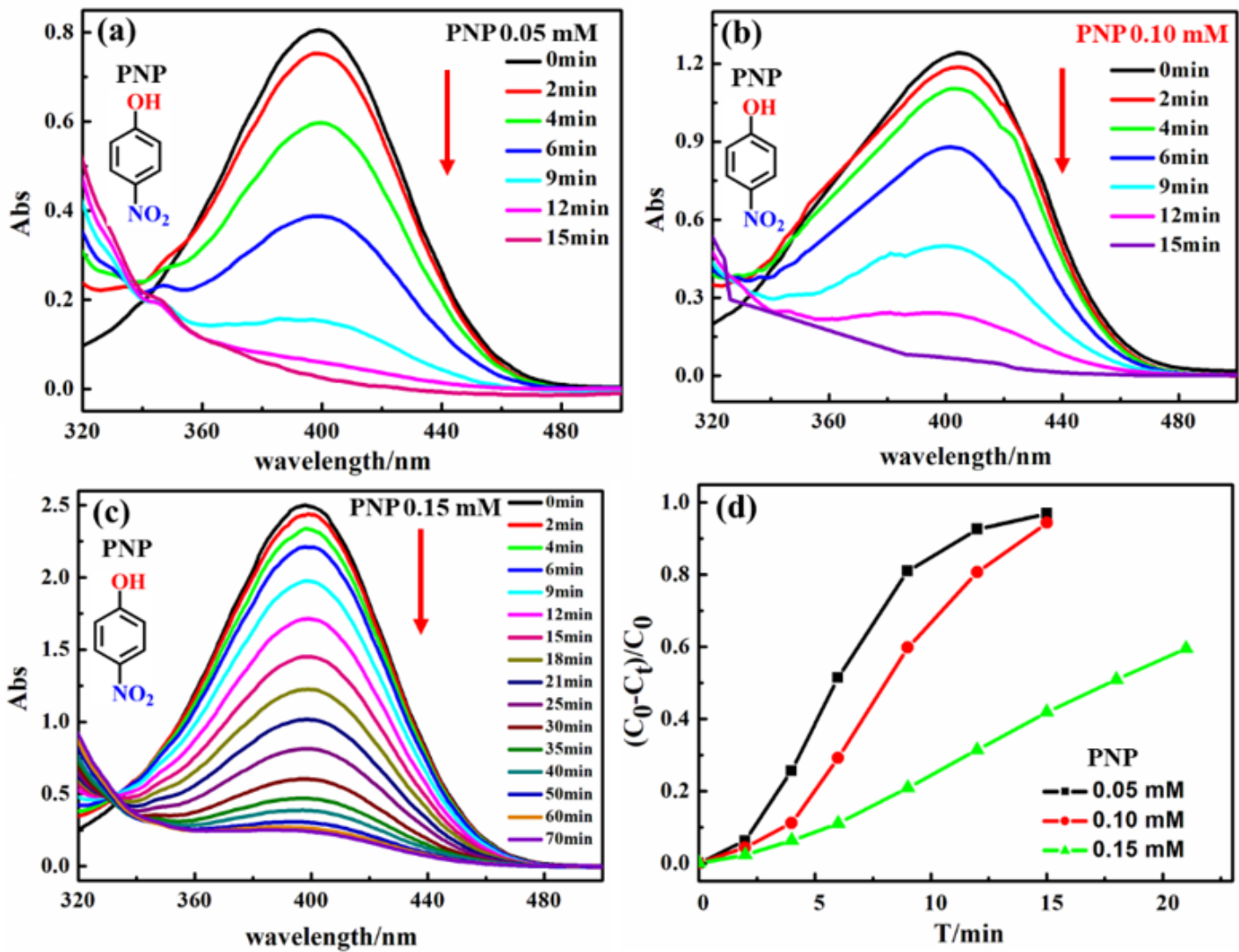


Figure 13

Effect of PNP concentration on catalytic reduction of PNP with 1: (a) 0.05 mM; (b) 0.1mM; (c) 0.15 mM; (d) Comparison of removal rates

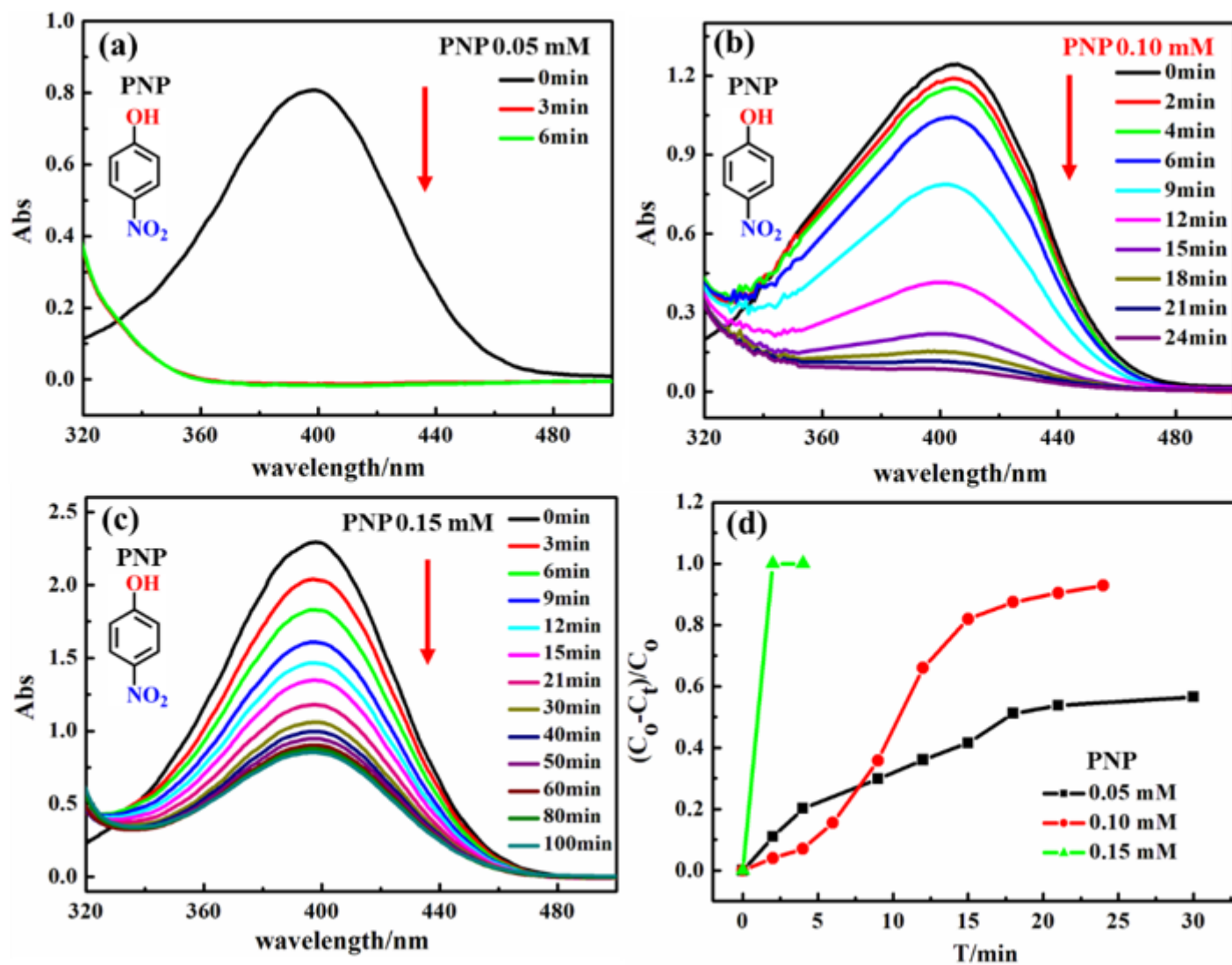


Figure 14

Effect of PNP concentration on catalytic reduction of PNP with 2: (a) 0.05 mM; (b) 0.1 mM; (c) 0.15 mM; (d) Comparison of removal rates

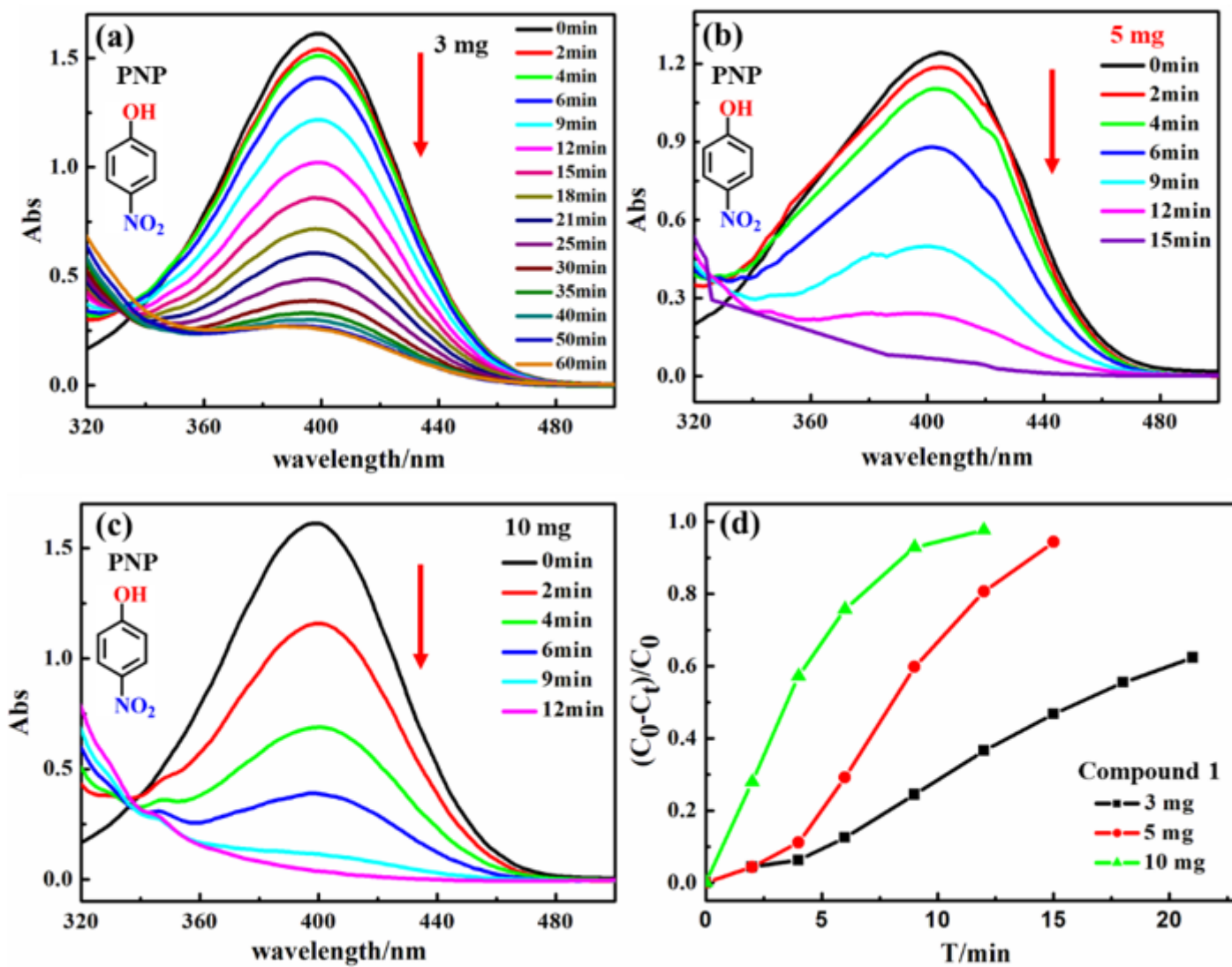


Figure 15

Effect of compound dose on catalytic reduction of PNP with 1: (a) 3 mg; (b) 5 mg; (c) 10 mg; (d) Comparison of removal rates of PNP in catalytic reduction of 1 with compound dose

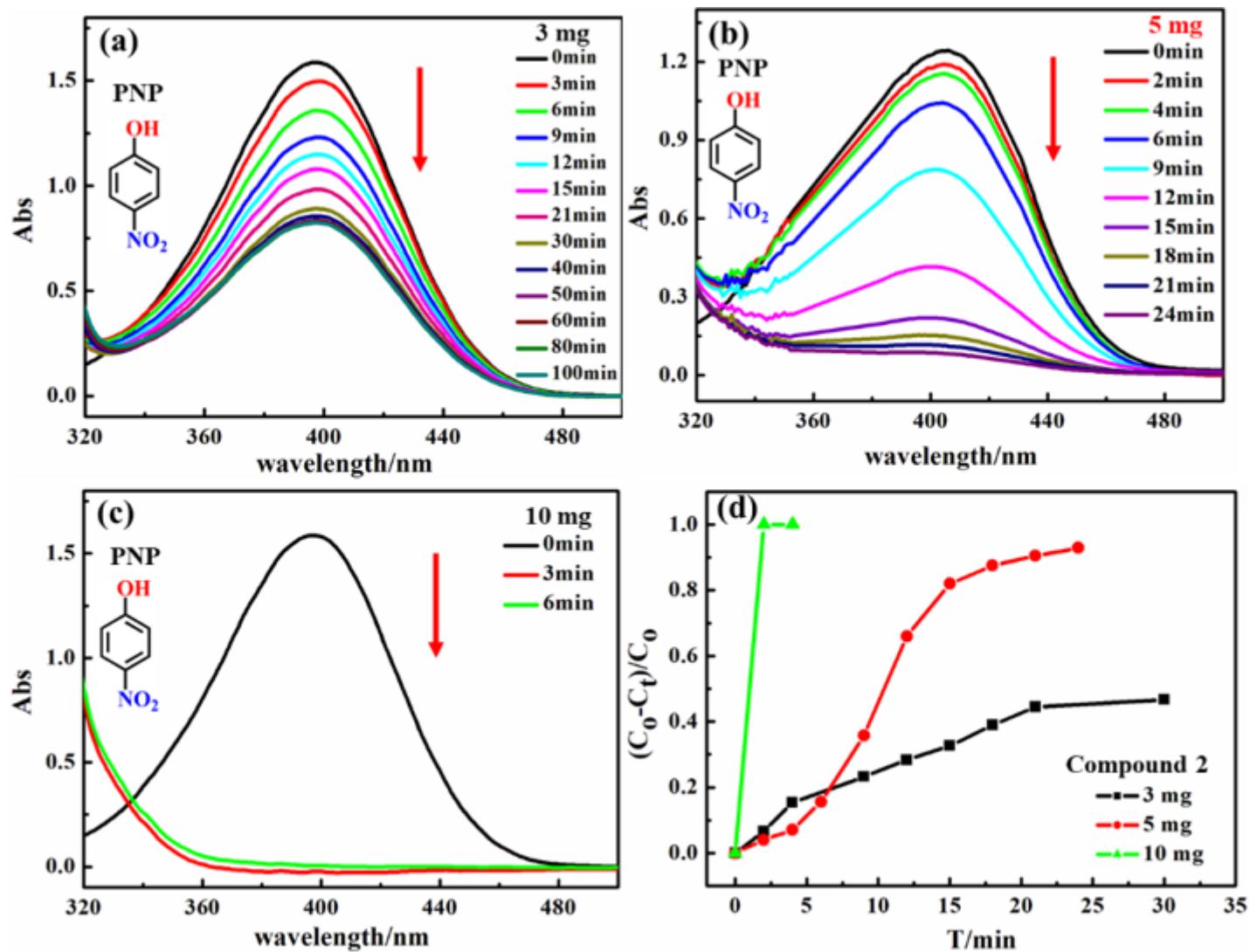


Figure 16

Effect of compound dose on catalytic reduction of PNP with 2: (a) 3 mg; (b) 5 mg; (c) 10 mg; (d) Comparison of removal rates of PNP in catalytic reduction of 2 with compound dose

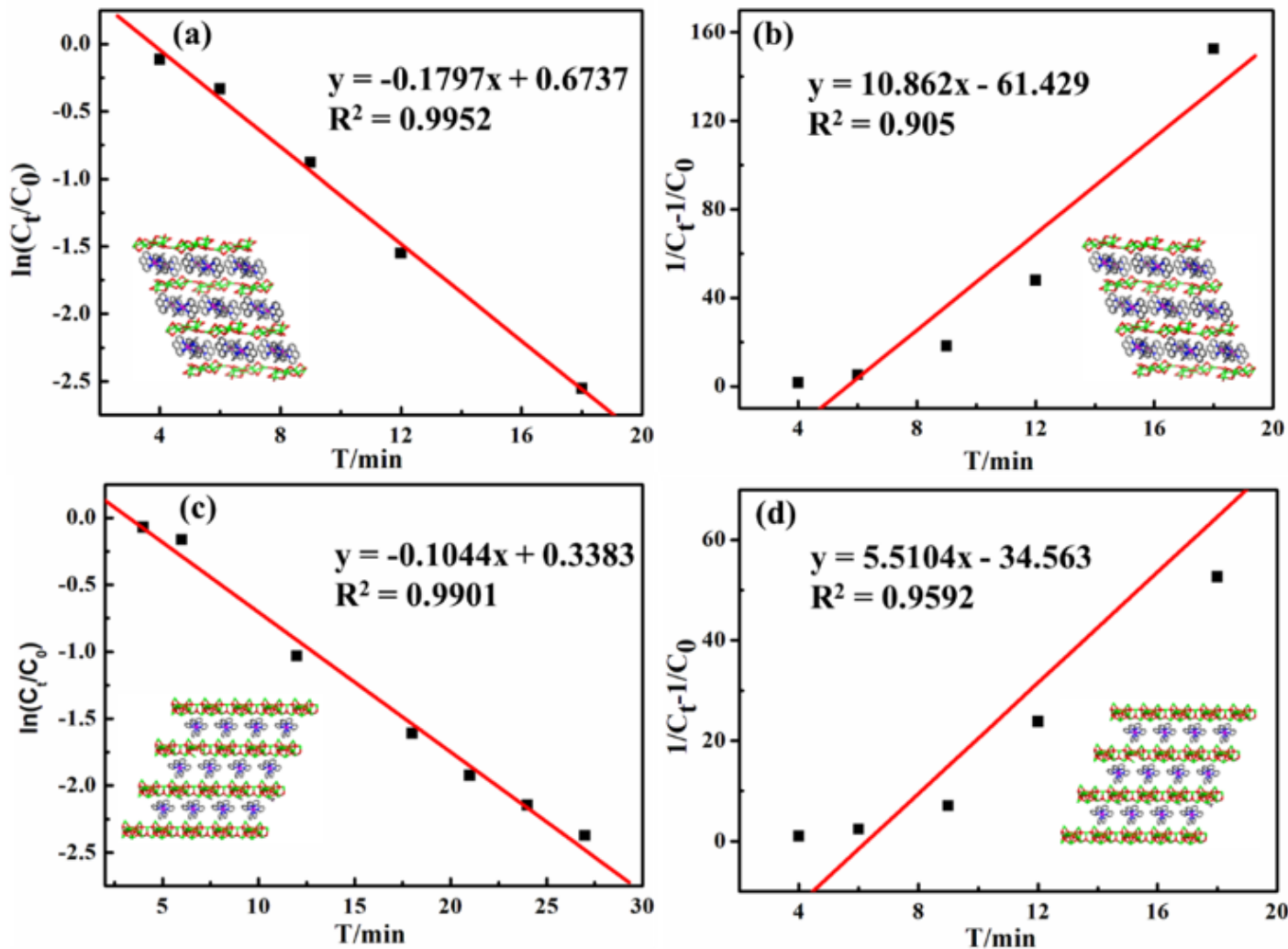


Figure 17

(a) Pseudo-first-order kinetic curves of catalytic reduction of PNP with 1; (b) Pseudo-second-order kinetic curves of catalytic reduction of PNP with 1; (c) Pseudo-first-order kinetic curves of catalytic reduction of PNP with 2; (d) Pseudo-second-order kinetic curves of catalytic reduction of PNP with 2

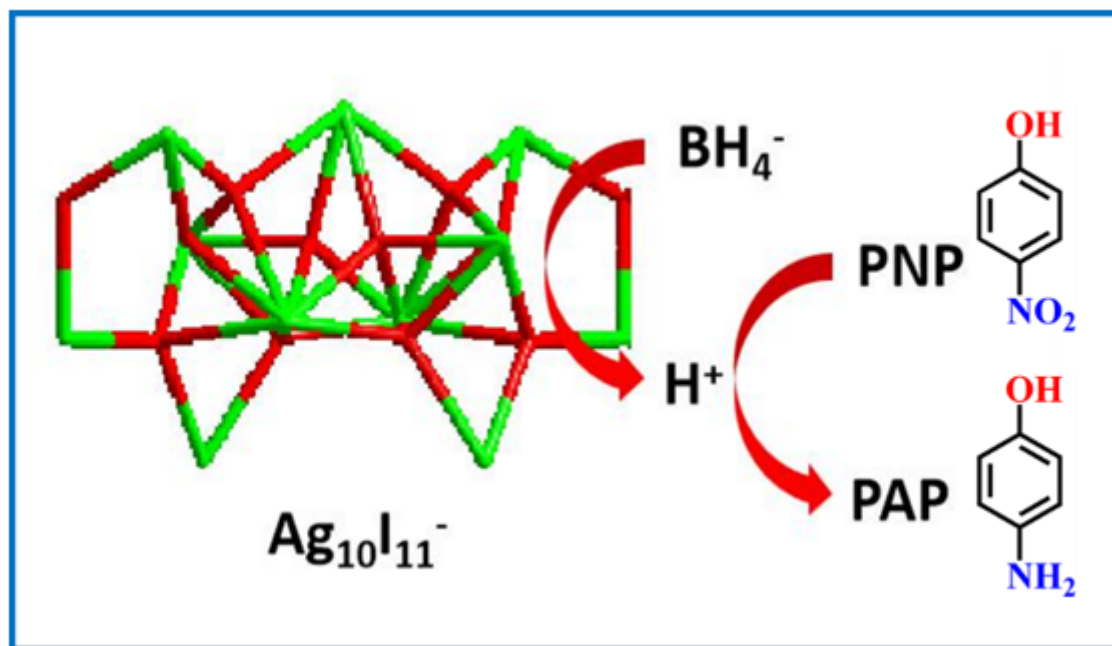


Figure 18

Mechanism of catalytic reduction of PNP

Supplementary Files

This is a list of supplementary files associated with this preprint. Click to download.

- [1.pdf](#)
- [2.pdf](#)
- [Supportinginformation.docx](#)
- [TOC.docx](#)